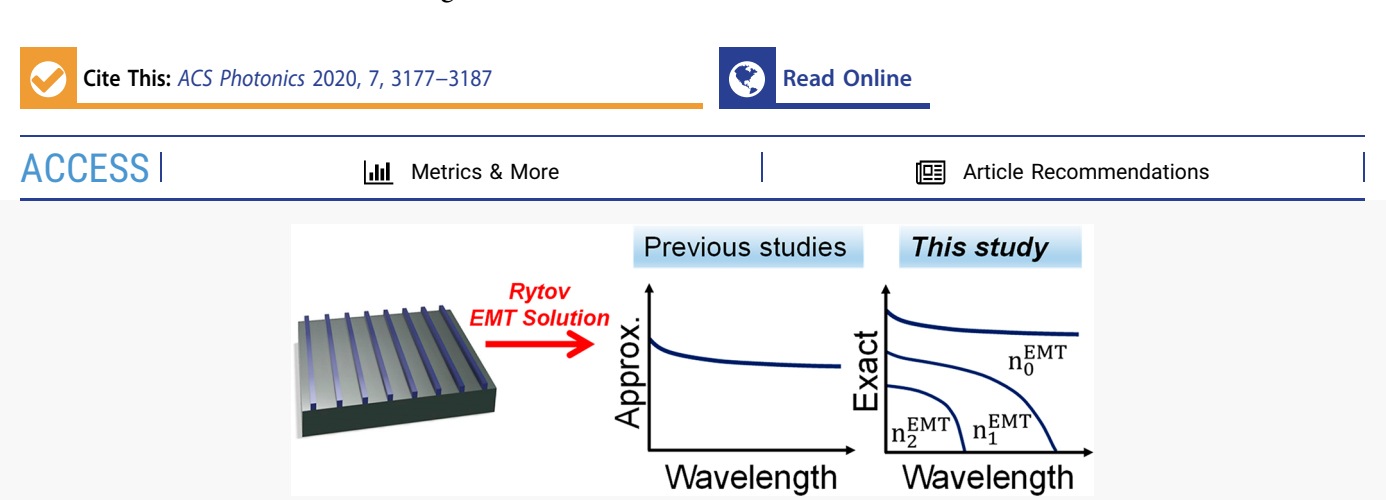


pubs.acs.org/journal/apchd5 Article

Applicability of Rytov's Full Effective-Medium Formalism to the Physical Description and Design of Resonant Metasurfaces

Hafez Hemmati and Robert Magnusson*



ABSTRACT: Periodic photonic lattices constitute a fundamental pillar of physics supporting a plethora of scientific concepts and applications. The advent of metamaterials and metastructures is grounded in a deep understanding of their properties. Based on Rytov's original 1956 formulation, it is well-known that a photonic lattice with deep subwavelength periodicity can be approximated with a homogeneous space having an effective refractive index. Whereas the attendant effective medium theory (EMT) commonly used in the literature is based on the zeroth root, Rytov's closed-form transcendental equations possess, in principle, an infinite number of roots. Thus far, these higher-order solutions have been totally ignored; even Rytov himself discarded them and proceeded to approximate solutions for the deep-subwavelength regime. In spite of the fact that Rytov's EMT models an infinite half-space lattice, it is highly relevant to modeling practical thin-film periodic structures with a finite thickness as we show. Therefore, here, we establish a theoretical framework to systematically describe subwavelength resonance behavior and to predict the optical response of resonant photonic lattices using the full Rytov solutions. Expeditious results are obtained because of the semianalytical formulation with direct, new physical insights available for resonant lattice properties. We show that the full Rytov formulation implicitly contains refractive-index solutions pertaining directly to evanescent waves that drive the laterally propagating Bloch modes foundational to resonant lattice properties. In fact, the resonant reradiated Bloch modes experience wavelength-dependent refractive indices that are solutions of Rytov's expressions. This insight is useful in modeling guided-mode resonant devices including wideband reflectors, bandpass filters, and polarizers. For example, the Rytov indices define directly the bandwidth of the resonant reflector and the extent of the bandpass filter sidebands as verified with rigorous simulations. As an additional result, we define a clear transition point between the resonance subwavelength region and the deep-subwavelength region with an analytic formula provided in a special case.

KEYWORDS: effective medium theory, periodic subwavelength metasurfaces, wideband reflector, bandpass filter, polarizer, waveguide modes

Periodic photonic lattices, known as diffraction gratings for 100 years and diffractive optical elements for decades, have a venerable history. ¹⁻⁵ With major discoveries in optical physics deriving from their deployment, periodic structures enable wide application fields, including spectroscopy, laser technology, and sensors. Imbuing the lattice with waveguiding capability offers yet another set of functionalities grounded in resonance effects due to excitation of lateral leaky Bloch modes. ⁶⁻¹⁴ In the recent past, periodic photonic lattices are often referred to as "metasurfaces" or "metamaterials" in which periodically aligned wavelength-scale features enable manipulation of an incoming electromagnetic waves in a desired manner. ¹⁵⁻¹⁹ Resonant lattices offer novel properties and light-

wave control in compact format potentially replacing and complementing conventional optical devices.

Extensive theoretical and experimental studies have been conducted to realize resonant and nonresonant periodic structures in materials systems pertinent to the various spectral regions. Whereas various wavelength (λ) to periodicity (Λ)

Received: August 5, 2020 Published: November 8, 2020





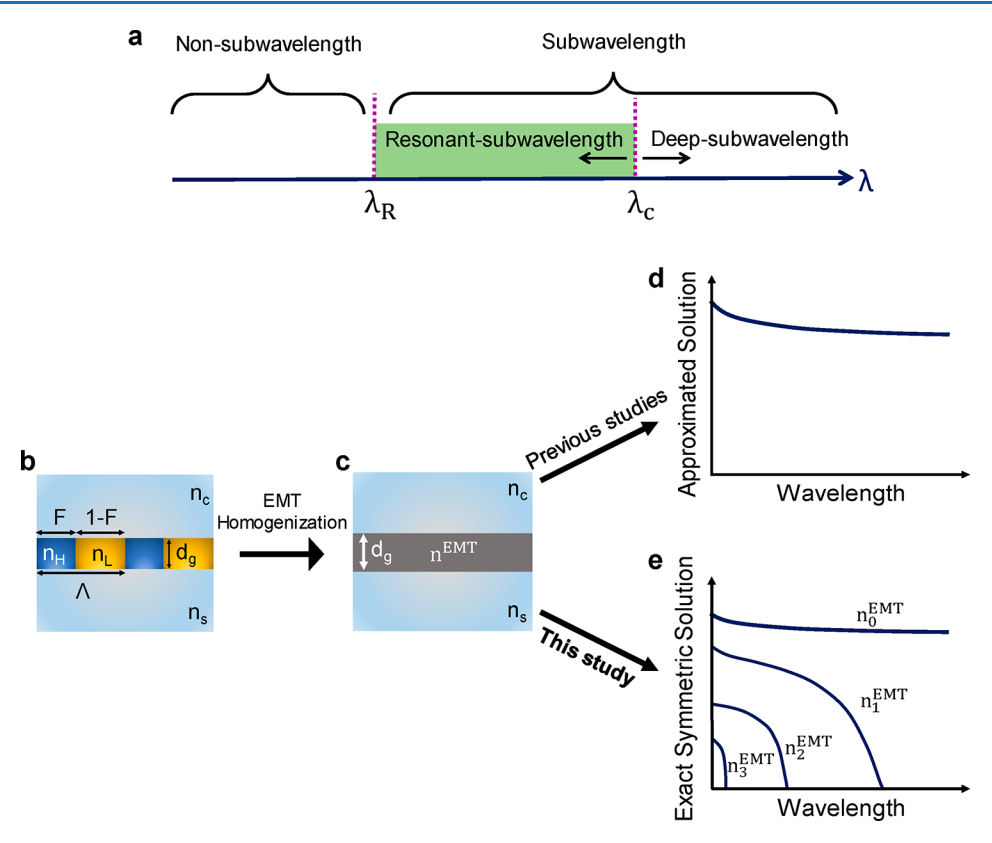


Figure 1. Schematics illustrating (a) the diffraction regimes pertaining to Rytov's solutions, (b) the general rectangular grating model, (c) equivalent thin-film EMT model, (d) the zeroth-root Rytov solution basic to all past EMT models, and (e) calculated effective refractive indices presented in this study based on the exact Rytov formalism.

ratios can be deployed, working in the subwavelength regime offers a particularly efficient optical response. Transition from the nonsubwavelength to the subwavelength regime occurs at the Rayleigh wavelength (λ_R) .² For wavelength values longer than λ_R , all higher diffraction orders are eliminated and only the zero orders propagate in the cover and substrate media. In the subwavelength regime, one can define two main regions. These are the deep-subwavelength region where the wavelength is much larger than the period, showing thin-film effects on account of a high degree of homogenization, and the resonant subwavelength region where the wavelength-scale periodicity triggers guided-mode, or leaky-mode, resonance effects. These regions are shown schematically in Figure 1a. While the Rayleigh wavelength is known by $\lambda_R = n_S \Lambda$, there exists no definition for this transition wavelength that we refer to as a cutoff wavelength (λ_c); here, we propose a definition for this value

Since the seminal work by Rytov in 1956, the effective refractive indices of subwavelength gratings can be calculated for both transverse electric (TE) and transverse magnetic (TM) polarization states. His effective-medium theory (EMT) applies to an infinite periodic halfspace. Treating continuity and periodicity of the electromagnetic fields at boundaries between constituent materials in a unit cell results in polarization-dependent transcendental equations. Employing a series expansion for the tangent term in the transcendental equations returns the well-known zero-order, second-order, or higher-order approximate solutions for effective refractive indices. Applying EMT based on the approximated Rytov formulation, one can replace a subwavelength grating by an equivalent homogeneous film with

corresponding effective refractive indices for each polarization. This process is noted schematically in Figures 1b,c. The thickness of the homogeneous film is identical to the grating thickness. In the deep subwavelength, or quasi-static, limit λ/Λ $\rightarrow \infty$, the zero-order effective refractive indices result in a reliable solution in terms of equivalent reflection, transmission, and phase calculations. Notably, in 1986, Gaylord et al. implemented zero-order EMT to approximate subwavelength gratings with a single homogeneous layer in order to design an antireflection coating at normal incidence.²¹ In a related work, Ono et al. approximated a sinusoidal ultrahigh spatial frequency grating by several rectangular grating layers with different fill factors to design an antireflection structure.²² They calculated the refractive index of each rectangular layer using the zero-order approximation. However, the zero-order approximation fails for wavelengths outside the deep subwavelength regime. Therefore, as the value of λ/Λ approaches the resonant subwavelength regime (i.e., $\lambda \sim \Lambda$) higher-order approximations must be used. Thus, Richter et al. used second-order EMT to design and study optical elements with a form birefringent structure.²³ Moreover, Raguin and Morris utilized second-order EMT to design antireflection surfaces in the infrared (IR) electromagnetic bands.²⁴

All previous EMT studies^{21–29} based on Rytov's formulation,²⁰ with either exact or approximated solutions, have reported only one effective refractive index for each wavelength, as depicted in Figure 1d. In contrast, here, we report that solving the exact transcendental equation in the resonant subwavelength regime can result in several effective refractive indices for a single wavelength. Mathematically, since $\tan(x)$ has an infinite sets of roots, this may not come as a surprise.

What is surprising is that these roots are highly applicable to practical problems modeling photonic lattices with finite thickness, namely, metasurfaces and metameterials, as we show in detail in the remainder of the paper. These higher-order solutions have been completely ignored thus far to our knowledge. Even Rytov himself paid no attention to them and proceeded to derive simplified approximate expressions based on the zeroth root.²⁰ In his case, this is understandable, as resonant photonic lattices were not known at that time.

Henceforth, we establish our theoretical framework to systematically describe subwavelength resonance behavior and predict the optical response of resonant photonic lattices using the full Rytov solutions. Expeditious results are obtained because of Rytov's semianalytical formulation with direct, new physical insights available for resonant lattice properties. To prove the correctness of the proposed approach, we compare our semianalytical results with rigorously computed results and show excellent agreement between them. Our solutions, based on the exact symmetric Rytov problem, are previewed schematically in Figure 1e. Most importantly, we show here that the higher Rytov solutions $n_m^{\rm EMT}$ correspond exactly to reradiated fields generated by higher-order evanescent diffracted waves represented as S_m , $m=\pm 1$, ± 2 , ..., driving the resonance process. $^{30-32}$

RYTOV REFRACTIVE INDICES AND THEIR INTERPRETATION

We first review the Rytov formalism²⁰ for TE polarization, where the electric-field vector is parallel to the grating lines. The full formula for a rectangular grating structure with infinite thickness is derived by considering the continuity of the electric and magnetic fields at boundaries between the ridges and grooves. There results a transcendental equation given by

$$(1 + \kappa^2)\sin(\alpha_1 a)\sin(\alpha_2 b) + 2\kappa(1 - \cos(\alpha_1 a)\cos(\alpha_2 b)) = 0$$
(1)

where $\alpha_1=k_0\sqrt{n_{\rm H}^2-(n_{\rm TE}^{\rm EMT})^2}$, $\alpha_2=k_0\sqrt{n_{\rm L}^2-(n_{\rm TE}^{\rm EMT})^2}$, $k_0=2\pi/\lambda_0$, $\kappa=\alpha_1/\alpha_2$, and $n_{\rm TE}^{\rm EMT}$ represent the effective refractive index for the TE case. The parameters a and b are the widths of the grating constituents with refractive indices $n_{\rm H}$ and $n_{\rm L}$, respectively. Based on this, one can define parameters $F=a/\Lambda$ and $1-F=b/\Lambda$ as fill factors of each section in a unit cell, as shown in Figure 2a. Since symmetric rectangular gratings are

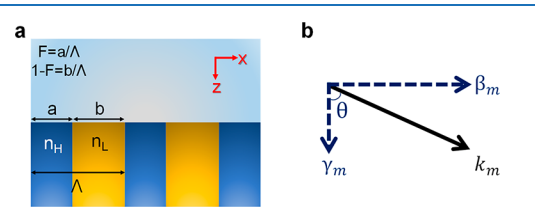


Figure 2. (a) Schematic of the half space grating model in Rytov's formulation with an infinite number of periods along the X direction. (b) Wavevector of the mth diffracted order accompanied by its vertical (Z direction) and horizontal (X direction) components.

considered in Rytov's model, he extracted solutions from the full formula, eq 1, that are pertinent to symmetric field distributions inside the grating. Accordingly, eq 1 is reduced to eq 2, which we reference here as the "exact" Rytov formulation for TE polarization.

$$\sqrt{n_{\rm L}^2 - (n_{\rm TE}^{\rm EMT})^2} \ \tan \left[\frac{\pi \Lambda}{\lambda} (1 - F) \sqrt{n_{\rm L}^2 - (n_{\rm TE}^{\rm EMT})^2} \right]
= -\sqrt{n_{\rm H}^2 - (n_{\rm TE}^{\rm EMT})^2} \ \tan \left[\frac{\pi \Lambda}{\lambda} F \sqrt{n_{\rm H}^2 - (n_{\rm TE}^{\rm EMT})^2} \right]$$
(2)

Similarly, for TM polarization, where the magnetic-field vector is parallel to the grating lines, there results

$$\frac{\sqrt{n_{\rm L}^2 - (n_{\rm TM}^{\rm EMT})^2}}{n_{\rm L}^2} \tan\left[\frac{\pi\Lambda}{\lambda}(1 - F)\sqrt{n_{\rm L}^2 - (n_{\rm TM}^{\rm EMT})^2}\right]
= -\frac{\sqrt{n_{\rm H}^2 - (n_{\rm TM}^{\rm EMT})^2}}{n_{\rm H}^2} \tan\left[\frac{\pi\Lambda}{\lambda}F\sqrt{n_{\rm H}^2 - (n_{\rm TM}^{\rm EMT})^2}\right]$$
(3)

Solving the exact Rytov equations, eqs 2 and 3, for $n_{\rm TE}^{\rm EMT}$ and $n_{\rm TM}^{\rm EMT}$ delivers a set of effective refractive indices that depend on the wavelength and the input design parameters. In principle, due to the periodicity of $\tan(x)$, there exists an infinite number of solutions; in practice, a few of the lowest-order solutions will be useful. Except for $n_0^{\rm EMT}$, the effective refractive indices have specific cutoff wavelengths. Knowing the cutoff wavelengths is key to predicting the optical response as shown here. Working at wavelengths longer than the Rayleigh wavelength, $\lambda_R = n_{\rm S} \Lambda$, ensures zero-order propagation toward the cover and substrate with all higher-order diffracted waves being evanescent. These higher diffraction orders propagate in the periodic region depending on the structural design and corresponding cutoff values of λ_c^m .

In the periodic region, the fundamental coupled wave expansion of the y-component of the electric field can be written as 33,34

$$E_{y}(x, z) = \sum_{m} S_{m}(z) \exp[-i(k - mK)x)]$$
 (4)

where $S_m(z)$ are the amplitudes of the space-harmonic components in the Fourier series expansion of the total field in the periodic direction, k is the wave vector of a diffracted wave, and $K = 2\pi/\Lambda$ is the grating vector magnitude. Each diffracted order possesses a wavevector (k_m) in the direction of propagation which can be resolved into vertical and horizontal components, as depicted in Figure 2b. Effective refractive indices obtained by solving the Rytov equations pertain to the vertical components of the diffracted orders belonging to k_m . We have

$$k_m^2 = \beta_m^2 + \gamma_m^2 \tag{5}$$

where $\beta_m = k_m \sin \theta$, $\gamma_m = k_m \cos \theta$, $k_m = k_0 n_m (\lambda_0)$, and $k_0 = 2\pi/\lambda_0$. Defining $N_m(\lambda_0) = \beta_m/k_0 = n_m(\lambda_0) \sin \theta$ and $n_m^{\rm EMT}(\lambda_0) = \gamma_m/k_0 = n_m(\lambda_0) \cos \theta$, a relation is obtained between the component refractive indices of Figure 2b as

$$(n_m(\lambda_0))^2 = (N_m(\lambda_0))^2 + (n_m^{\text{EMT}}(\lambda_0))^2$$
 (6)

Here, n_m is the refractive index experienced by a diffracted wave with wavevector k_m . In the geometry of a periodic waveguide, N_m represents the lateral effective index seen by the $m^{\rm th}$ Bloch mode, whereas $n_m^{\rm EMT}$ refers to the vertical effective index seen by the resonant reradiated Bloch modes.

The objective of Figure 3 is to connect the Rytov model with practical device geometry as applied in metamaterials presently. Accordingly, Figure 3a shows an example grating membrane structure enclosed by air and its reflection spectrum mapped in wavelength versus grating thickness (d_o) . This

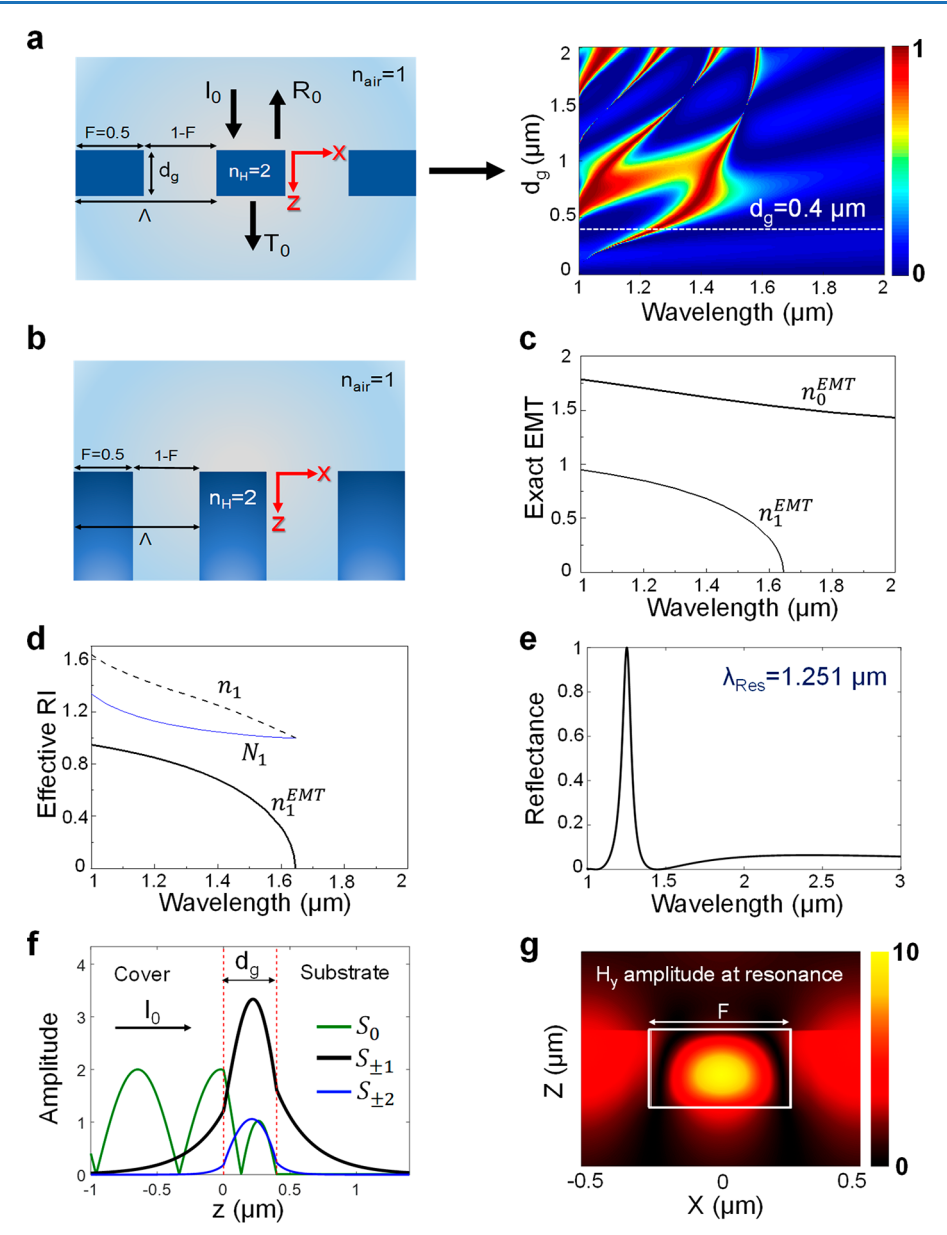


Figure 3. (a) Schematic of a representative grating membrane and corresponding RCWA-based reflection map as a function of grating thickness (d_g) for TM-polarized incident light, (b) schematic of the half-space grating model, (c) calculated exact effective refractive indices, (d) wavelength dependent effective refractive indices of waveguide (n_1) , horizontal component (N_1) , and vertical component $(n_1^{\rm EMT})$, based on eq 6, (e) simulated reflectance spectrum of a grating with $d_g = 0.4 \ \mu m$, (f) amplitude of the coupled diffracted orders at resonance wavelength of $\lambda_{\rm Res} = 1.251 \ \mu m$, and (g) distribution of total magnetic field in one period at the resonance wavelength of $\lambda_{\rm Res} = 1.251 \ \mu m$ showing TM₀ mode shape. The grating structure has constant parameters of $\Lambda = 1 \ \mu m$, F = 0.5, $n_{\rm H} = 2$, and $n_{\rm L} = n_{\rm c} = n_{\rm s} = 1$.

spectrum is computed with rigorous coupled-wave analysis (RCWA). 33,34 The corresponding half-space grating structure used in the Rytov model is presented in Figure 3b. The effective refractive indices $n_m^{\rm EMT}$ obtained by solving the exact Rytov eq 3 are shown in Figure 3c. The values of $n_m^{\rm EMT}$ denote vertical components of the refractive indices n_m that quasiguided evanescent-wave diffraction orders see in the direction of propagation in the periodic medium. These evanescent diffraction orders excite lateral leaky Bloch modes that generate the guided-mode resonance. Comparing the rigorously computed resonance map in Figure 3a to Figure 3c shows that no resonance occurs in the region where $n_1^{\rm EMT}=0$. Moreover, using eq 6 with values of $n_m^{\rm EMT}$ obtained by the exact Rytov formula, one can find the corresponding pairs of n_m and N_m satisfying the eigenvalue equation of the equivalent

homogeneous slab waveguide. Figure 3d depicts these values as a function of wavelength for an equivalent waveguide having a thickness of $d_{\rm g}=0.4~\mu{\rm m}$. It can be inferred from this figure that the cutoff wavelength occurs when the refractive index of the waveguide reaches $n_m=n_{\rm air}=1$ at which point the waveguide vanishes. Thus, at the cutoff wavelength, the refractive index contrast becomes zero such that no waveguide mode can be supported. For the grating design of Figure 3a, with $d_{\rm g}=0.4~\mu{\rm m}$, the resonance manifests as a reflection peak at $\lambda_{\rm Res}=1.251~\mu{\rm m}$, as shown in Figure 3e. At the resonance wavelength, one can compute with RCWA the amplitudes of the coupled diffracted orders and simulate the magnetic-field distribution, as shown in Figures 3f and g, respectively. It is clearly illustrated that the dominant contribution to the internal modal field, whose cross-section is shown in Figure 3f,

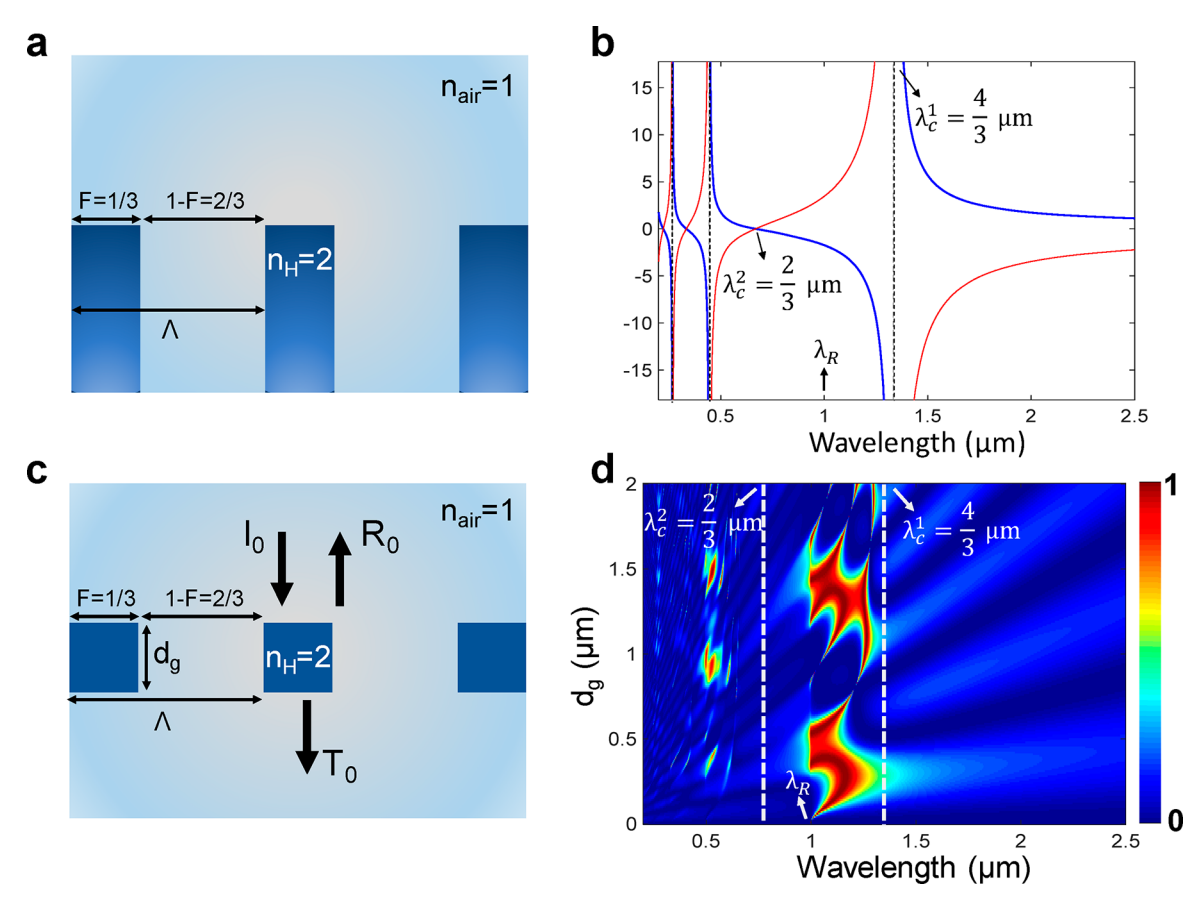


Figure 4. Grating design with parameters satisfying conditions for an analytic study. (a) Schematic of the half-space grating model, (b) graphical solution of eq 7 to find the cutoff wavelengths of the diffracted waves in the grating region, (c) schematic of a grating membrane with finite thickness, and (d) corresponding reflection map as a function of grating thickness (d_g).

is due to the evanescent diffraction orders with amplitudes $S_{\pm 1}$, which is also completely consistent with the total magnetic-field distribution illustrated in Figure 3g. Interestingly, this point can be predicted and explained directly via Figure 3c; as the resonance wavelength falls below the cutoff wavelength of the first diffracted order (λ_c^1) , we would expect the first diffracted orders $S_{\pm 1}(z)$ to be responsible for the resonance because it is this order that experiences $n_1^{\rm EMT}$.

■ RYTOV SOLUTIONS FOR CUTOFF WAVELENGTHS

Knowing the values for the cutoff wavelengths is important to distinguish the deep-subwavelength and resonant-subwavelength regions. Moreover, the cutoff wavelengths define the spectral location where a new evanescent diffraction order, with attendant lateral Bloch-mode excitation, enters and begins to participate in the resonance dynamics. The cutoff wavelengths λ_c^m occur when the vertical effective refractive index of diffraction order m vanishes (i.e., $n_m^{\rm EMT}=0$). The semianalytical Rytov formulas can be used to determine the first and higher cutoff wavelengths for any one-dimensional lattice. Therefore, plugging $n_{\rm TE}^{\rm EMT}=0$ into the exact Rytov formulation, for example, eq 2 for TE polarization, yields

$$n_{\rm L} \tan \left[\frac{\pi \Lambda}{\lambda} (1 - F) n_{\rm L} \right] = -n_{\rm H} \tan \left[\frac{\pi \Lambda}{\lambda} F n_{\rm H} \right]$$
 (7)

In general, there is no analytical solution for this equation. However, here we show that, for specific design parameters, one can straightforwardly and analytically calculate the cutoff wavelengths for each diffracted order. This works when the arguments of the tangent functions on each side of eq 7 become identical

$$(1 - F)n_{\rm L} = Fn_{\rm H} \tag{8}$$

Once this condition is satisfied, eq 7 holds for values of the tangent arguments equal to $m\pi/2$ (m=1, 2, 3, ...), which results in closed-form, simple analytical solutions

$$\lambda_{\rm c}^{\,m} = \frac{2}{m} \Lambda F n_{\rm H} \tag{9}$$

giving the cutoff wavelength for each diffraction order. All photonic lattices supporting guided-mode resonance admit at least the first evanescent diffraction order. Thus, with m=1, we get $\lambda_c^1=2\Lambda F n_{\rm H}$. This is a remarkable canonical result. From eq 8, appropriate fill factors satisfying these solutions are $F=n_{\rm L}/(n_{\rm L}+n_{\rm H})$. These values of F are, therefore, reasonable for experimental realization. In the subwavelength regime, to ensure that at least one resonance arises from the $m^{\rm th}$ diffraction order, the Rayleigh wavelength should be smaller than the cutoff wavelength (i.e., $\lambda_R < \lambda_c^m$). This yields a constraint $F > n_{\rm s}/2n_{\rm H}$ for m=1. Previously, Lalanne et al. obtained a numerical solution for λ_c^1 and pointed out its analogy with the Rayleigh wavelength. One significant point in our solution is that the cutoff wavelengths are fixed and will not change with changes in the refractive index of the cover and substrate.

In this spirit, one can engineer the spectral response and the number of diffracted orders at work by appropriately choosing the values of λ_R and λ_c^m for grating design. For example, the

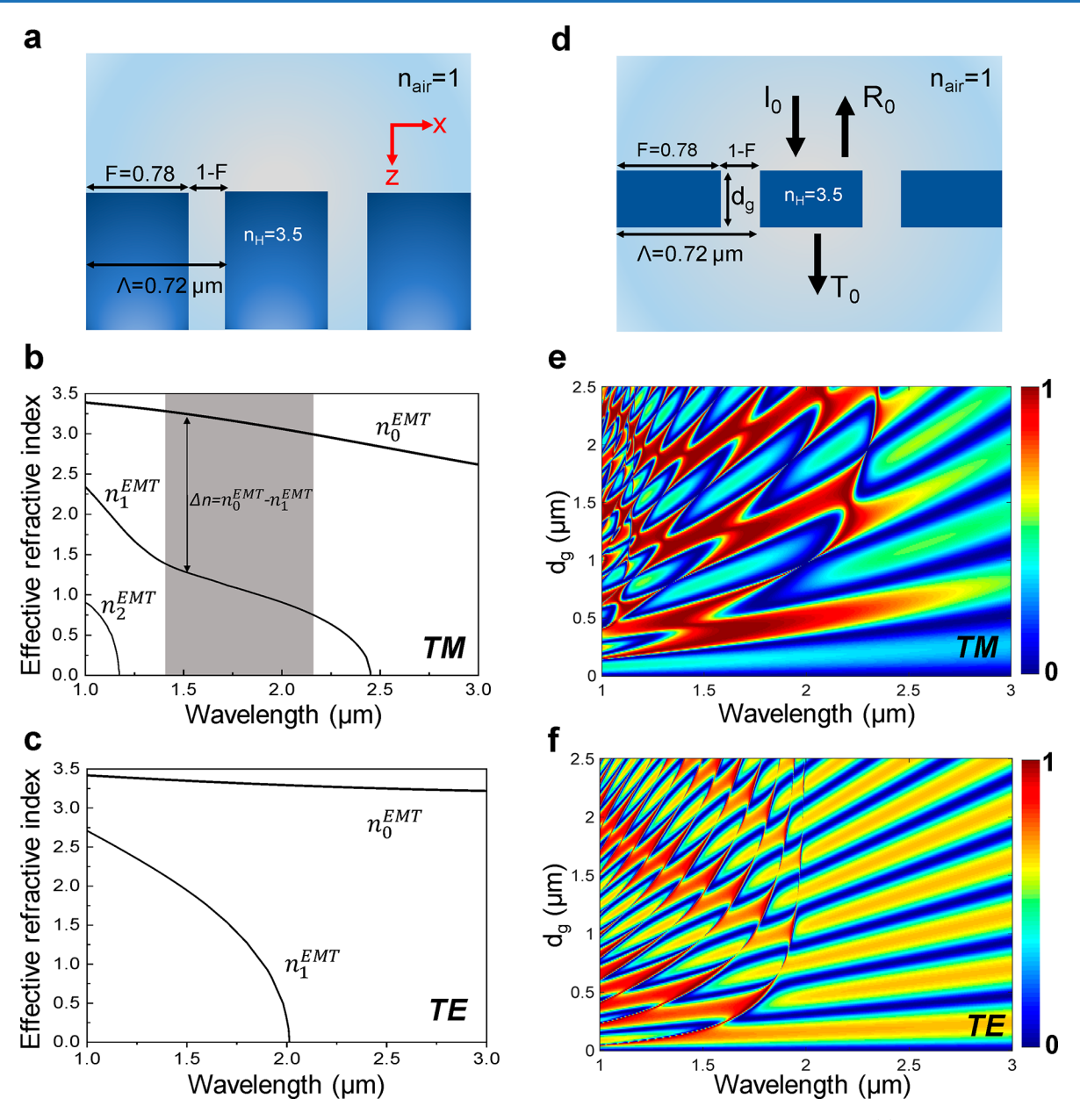


Figure 5. An example demonstrating the use of the Rytov indices for design of a wideband resonant reflector. (a) Schematic of the half-space model. Calculated effective refractive indices using the Rytov formalism for (b) TM-polarization and (c) TE-polarization states. (d) A schematic of a corresponding grating membrane with parameters $\Lambda=0.72~\mu\text{m}$, F=0.78, $n_{\text{H}}=3.5$, and $n_{\text{L}}=n_{\text{air}}=1$. Simulated reflection maps in wavelength vs grating thickness (d_{g}), pertinent to normally incident (e) TM-polarized and (f) TE-polarized light. In the maps, the dark red color implies R_0 approaching 1.

grating design depicted in Figure 4a, having parameters F=1/3, $\Lambda=1~\mu\text{m}$, $n_{\rm H}=2$, and $n_{\rm L}=1$, satisfies eq 8. Thus, the cutoff wavelengths for each evanescent diffracted order can be obtained analytically, as expressed in eq 9, which returns values of $\lambda_{\rm c}^1=4/3\sim1.33~\mu\text{m}$ and $\lambda_{\rm c}^2=2/3\sim0.66~\mu\text{m}$ for the first two orders. The Rayleigh wavelength of this design is $\lambda_{\rm R}=1~\mu\text{m}$, which is smaller than the first-order cutoff wavelength $\lambda_{\rm c}^1=4/3\sim1.33~\mu\text{m}$.

To validate the accuracy of our method, it is seen in Figure 4b that graphical solutions of eq 7 give the exact same values as obtained analytically by eq 9. Figure 4c shows a schematic of a grating membrane surrounded by air $(n_{\rm air}=1)$ with a finite thickness of $d_{\rm g}$. For this design, the cutoff wavelengths shown by dashed lines in Figure 4d, which is a RCWA-simulated

reflection map, are in full agreement with the analytical cutoff values.

RELEVANCE OF RYTOV'S FORMULATION TO RESONANCE DEVICE DESIGN

In this section, we show that the Rytov effective refractive indices are directly applicable to design of periodic photonic devices, including metamaterials and metasurfaces. Their deployment fully supports prior explanations of resonance device physics in terms of lateral leaky Bloch modes and guided-mode resonance.^{30–32} Their existence and spectral expressions are not consistent with resonance effects caused by local modes, including Fabry–Perot resonance or Mie scattering.^{35,36} Here, we treat example devices whose spectra

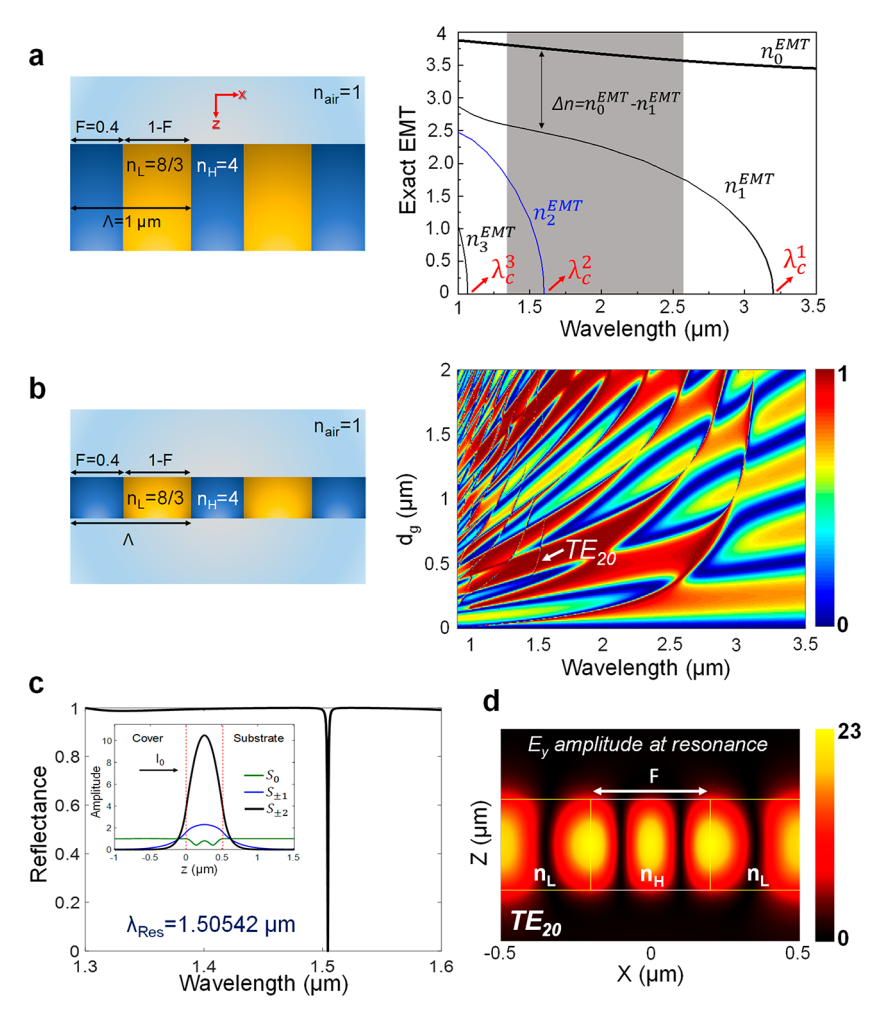


Figure 6. Rytov indices in bandpass filter analysis and design. The example filter works in TE polarization with parameters of $\Lambda=1~\mu\text{m}$, F=0.4, $n_{\rm H}=4$, $n_{\rm L}=8/3$, and $n_{\rm air}=1$. (a) Schematic of the Rytov half-space model and calculated effective refractive indices. (b) Schematic of the attendant grating membrane with finite thickness and its simulated reflection map as a function of grating thickness ($d_{\rm g}$). (c) Bandpass filter response of the device with grating thickness of $d_{\rm g}=0.51~\mu\text{m}$. Inset in (c) shows the amplitudes of the coupling diffracted orders at the resonance wavelength of $\lambda_{\rm Res}=1.50542~\mu\text{m}$. (d) Electric field distribution at resonance exhibiting a TE₂₀ profile.

and functionality are directly explainable using the Rytov indices.

■ WIDEBAND RESONANT REFLECTOR

One particularly useful device is the wideband resonant reflector in which nanopatterned design provides high reflectivity approaching 100% over a wide wavelength range. 31,37 Numerous studies have addressed these compact, often single-layer, reflectors both theoretically and experimentally for various optical wavebands. 10,32,36-40 Here, we apply the Rytov indices to substantiate the physical basis for the wideband reflection behavior. In this context, the half-space grating structure with parameters shown in Figure 5a is considered for the analysis. Corresponding roots of the exact Rytov equations for both TM and TE polarization states are found and the results are shown in Figures 5b and c, respectively. Similar curves were obtained by Lalanne et al. 10 using an RCWA-based numerical algorithm. For the TM case shown in Figure 5b, there are two significant points to be considered. The first one concerns the values of the cutoff wavelengths for each guided diffracted order and the second pertains to the shape of the index curves. For instance, it is illustrated in Figure 5b that in the wavelength range of 1.25 to

3 μ m, beyond the cutoff wavelength of the second order, only n_0^{EMT} and n_1^{EMT} exist in the effective refractive index diagram. Consequently, these two orders with m = 0 and m = 1 are responsible for all important spectral properties. Furthermore, it is seen that the slopes of the curves are almost identical with both curves varying monotonically in a wide wavelength range depicted by the gray region in Figure 5b. This is a key point to achieve wideband reflector response as the wavelengthdependent phase difference $(\Delta \varphi)$ accumulated in the zdirection between these two orders at work is defined by $\Delta \phi$ = $(2\pi/\lambda_0)(n_0^{\rm EMT}(\lambda_0)-n_1^{\rm EMT}(\lambda_0))d_{\rm g}$, which is proportional to the effective refractive-index difference of the first two orders obtained by the exact Rytov expression. Therefore, our method enables prediction as to whether to expect a wideband reflector behavior from a one-dimensional grating structure, simply by calculating effective refractive index graphs without performing any rigorous numerical simulations. The closed-form Rytov formulas might thus substantiate efficient design methods. Applying this approach to Figure 5c, it is seen directly that no wideband reflection response will arise out of this design for TE polarization as the slopes of the two curves differ significantly. To confirm our hypothesis, we performed RCWA-based simulations for the structure shown in Figure

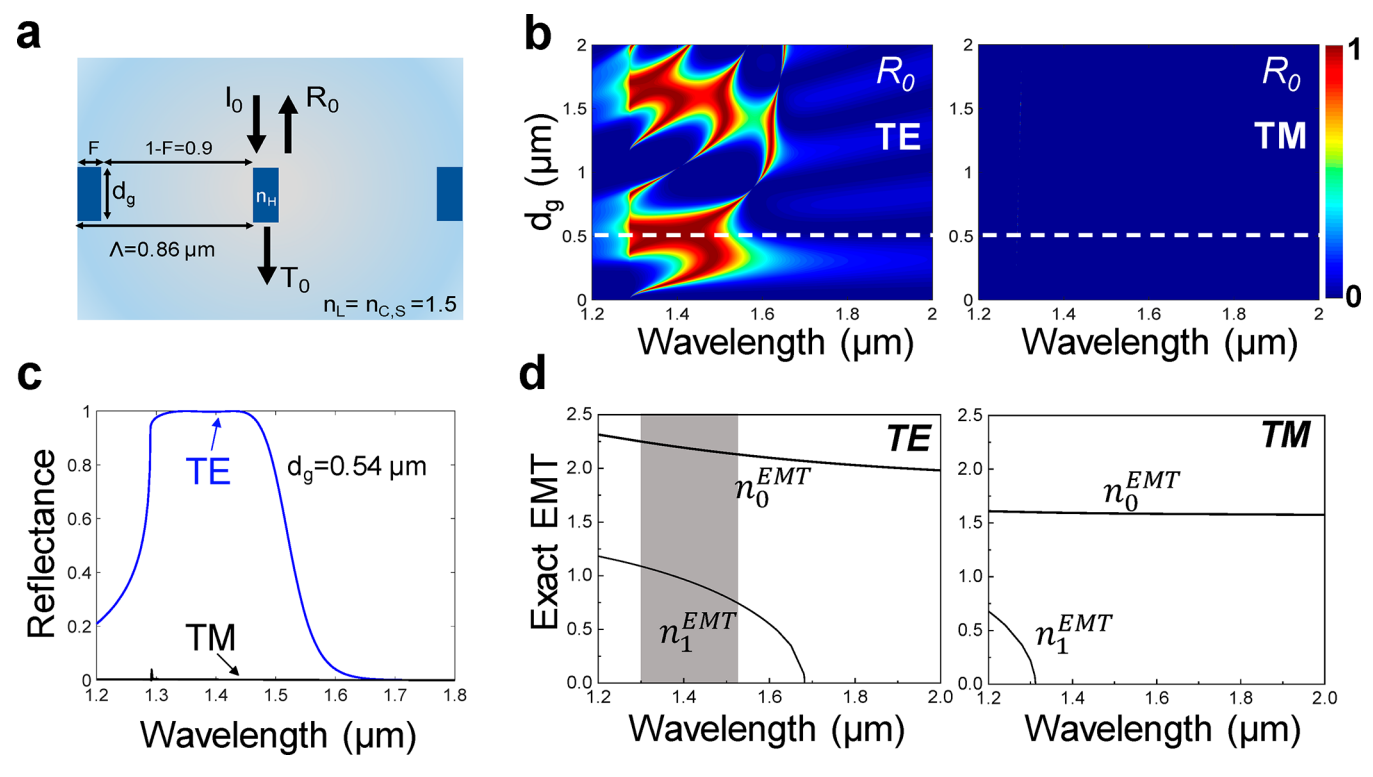


Figure 7. Rytov analysis of a sparse grating polarizer with parameters $\Lambda = 0.86 \ \mu\text{m}$, F = 0.1, $n_{\rm H} = 3.5$, and $n_{\rm L} = 1.5$ extracted from ref 46. (a) Schematic of the design with finite grating thickness of $d_{\rm g}$, (b) RCWA-based $\lambda - d_{\rm g}$ reflection map for TE and TM polarization states, (c) zero-order reflectance (R_0) spectra with $d_{\rm g} = 0.54 \ \mu\text{m}$, and (d) exact Rytov effective refractive index diagram for TE and TM cases.

Sd. Simulated zero-order reflection maps of this grating design for TM and TE cases are shown in Figure 5e and f, respectively. These maps validate our predictions of wideband reflection response occurring in TM polarization but no wideband reflection response for the TE case. Wideband reflectors are related to the regions with dark red colors in a wide wavelength range. These appear in the TM map at some specific grating thicknesses, $d_{\rm g}$, which provide an appropriate phase difference (completely in phase) for high reflection since $\Delta \varphi \propto d_{\rm g}$. Explanation of wideband resonance reflection applying the spectral phase pertinent to similar, albeit numerically simulated, effective indices was first provided by Lalanne et al. ¹⁰

■ GUIDED-MODE RESONANT BANDPASS FILTER

Another important grating-based optical device is the sparse, single-layer bandpass filter (BPF) exhibiting low transmission sidebands and a high-efficiency narrow-band transmission peak. 41–44 Low transmission sidebands and a transmission resonance peak correspond to a wideband high-reflection background and a reflection resonance dip, respectively. To study this device type, a half-space model and the corresponding calculated Rytov refractive indices are shown in Figure 6a. We chose the grating parameters to satisfy eq 8 to analytically obtain the cutoff wavelengths. As in the explanation of the wideband reflector, similarity in the slopes of the n^{EMT} curves enables an appropriate phase difference to obtain high reflectivity at a specific device thickness.

Thus, we expect a wideband reflector response in the wavelength range where $\Delta n/\lambda_0$ is relatively constant. This condition prevails in the gray region of the EMT graph of Figure 6a. This figure is significantly different from Figure 5b in that the gray region in Figure 5b contains only $n_0^{\rm EMT}$ and $n_1^{\rm EMT}$,

whereas the gray region in Figure 6a encompasses $n_0^{\rm EMT}$, $n_1^{\rm EMT}$, and $n_2^{\rm EMT}$. As $n_0^{\rm EMT}$ and $n_1^{\rm EMT}$ are responsible for a wideband reflection background, bringing the second order $n_2^{\rm EMT}$ to work will manifest as a reflection dip resonance feature in the optical spectrum because it exists within a region of total reflection. Figure 6b shows a schematic of the membrane version of the half-space grating design of Figure 6a and its reflection map as a function of grating thickness. The reflection map agrees well with the analytic solutions for the cutoff wavelengths and with the number of orders at work experiencing n_0^{EMT} , n_1^{EMT} , and $n_2^{\rm EMT}$. The resonance feature predicted based on the existence of the n_2^{EMT} curve in the effective refractive index graph is marked as TE₂₀ in the reflection map of Figure 6b. Figure 6c confirms a bandpass filter response having a wideband high reflection background. At the reflection dip wavelength, the inset in Figure 6c reveals that the second evanescent diffraction order m = 2 is dominant, showing that a nonzero n_2^{EMT} is key to realizing a bandpass filter. The electric field distribution at the resonance wavelength shown in Figure 6d furthermore indicates TE₂₀ response (fundamental mode excited by the second evanescent order), consistent with our model. In summary, the Rytov treatment of the resonant BPF is fully consistent with, and supports, prior descriptions of BPF physics. 41,42,44

■ GUIDED-MODE RESONANCE POLARIZER

The linear resonant polarizer is the final device example presented. In the past, it has been shown that ultracompact polarizers with high extinction ratios are realizable with resonant gratings. Treating here a known polarizer, the design schematic is shown in Figure 7a, displaying a small fill factor (F = 0.1), with $n_{\rm H} = 3.5$, embedded in a medium with a refractive index of 1.5 in a way that $n_{\rm L} = n_{\rm C} = n_{\rm S} = 1.5$ under

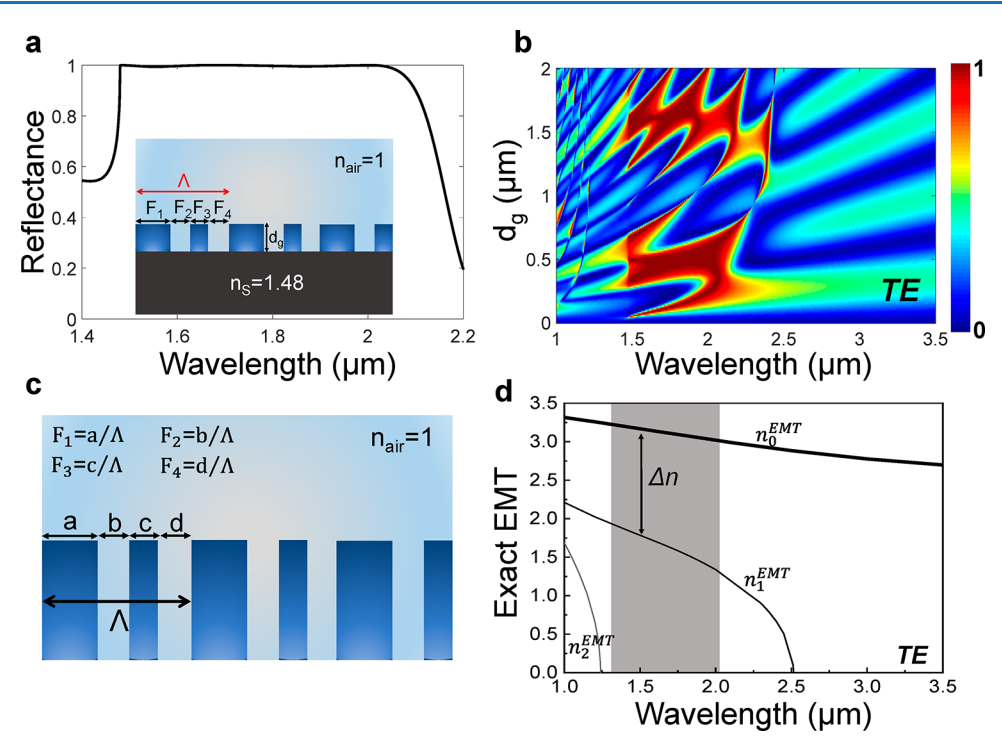


Figure 8. Effective refractive index analysis of a four-part unit cell grating with TE-polarized incident wave. (a) Wideband reflection spectrum of the four part grating on a substrate with $\Lambda=1~\mu\text{m}$, $F_1=0.075$, $F_2=0.275$, $F_3=0.375$, $F_4=0.275$, $n_S=1.48$, $n_C=1$, $n_H=3.48$, $n_L=1$, and $d_g=0.49~\mu\text{m}$, (b) wavelength vs grating thickness reflection map, (c) half-space model of the four-part structure, and (d) exact effective refractive indices for the TE case.

normal incidence. Figure 7b shows computed $\lambda - d_{\rm g}$ reflection maps for TE and TM polarization states. At the specific thickness of the grating denoted by the dashed line, TE polarization exhibits high reflection, while TM reflectance is suppressed. Reflectance spectra for a grating with thickness $d_{\rm g} = 0.54~\mu{\rm m}$, as shown in Figure 7c, reveal a good polarizing response in a wavelength range of 1.3–1.5 $\mu{\rm m}$. To elucidate the polarization behavior in the Rytov picture, we calculate TE and TM Rytov indices, as presented in Figure 7d. Again, the parallelism of the $n_0^{\rm EMT}$ and $n_1^{\rm EMT}$ curves in TE polarization enables a wideband reflector response. In contrast, for TM polarization in Figure 7d in the working range of the polarizer, only $n_0^{\rm EMT}$ exists. Consequently, we see that no guided-mode resonance features will occur in the TM case consistent with the simulated reflection map in Figure 7b.

APPLICATION TO METASURFACES WITH MULTIPART UNIT CELLS

Multipart unit cell metasurfaces have emerged as a promising platform to achieve exceptional properties not attainable with conventional two-part unit cell metasurfaces. For example, various novel functionalities can be obtained with four-part fill factor gratings, such as previously reported applications, including wideband antireflection, wideband reflection, large steering angle, and light-propelled spacecraft. With reference to Figure 8, writing down the conditions of continuity and periodicity of electric and magnetic fields for four-part grating designs, we find the following determinant expression:

$$\det \begin{bmatrix} \cos(\alpha_1 a) & \sin(\alpha_1 a) & -\cos(\alpha_2 a) & -\sin(\alpha_2 a) & 0 & 0 \\ 0 & 0 & \cos(\alpha_2 c) & -\cos(\alpha_1 c) & -\cos(\alpha_1 d) & \sin(\alpha_1 d) \\ \cos(\alpha_2 b) & -\kappa \sin(\alpha_2 b) & 0 & 0 & -\cos(\alpha_1 b) & \sin(\alpha_1 b) \\ \kappa \sin(\alpha_1 a) & -\kappa \cos(\alpha_1 a) & -\sin(\alpha_2 a) & \cos(\alpha_2 a) & 0 & 0 \\ 0 & 0 & \sin(\alpha_2 c) & -\cos(\alpha_2 c) & \kappa \sin(\alpha_1 d) & \kappa \cos(\alpha_1 d) \\ -\sin(\alpha_2 b) & -\kappa \cos(\alpha_2 b) & 0 & 0 & \kappa \sin(\alpha_1 b) & \kappa \cos(\alpha_1 b) \end{bmatrix} = 0$$
(10)

Solving this equation results in a set of effective refractive index values corresponding to the evanescent diffracted orders as discussed above. Results pertaining to an example four-part fill factor grating based on our theory are shown in Figure 8. A wideband reflector response of the finite thickness grating on a substrate under TE illumination is shown in Figure 8a. The

reflection map of the four-part structure as a function of the thickness of the grating is illustrated in Figure 8b. The infinite half-space design of the four-part period structure and corresponding effective refractive indices are depicted in Figure 8c and d, respectively. In complete agreement with our previous explanation for the conventional two-part

structure, the gray region in Figure 8 demonstrates near-constant values for $\Delta n/\lambda_0$ across the band, enabling the high reflectivity in this wide wavelength range. Therefore, the principles underlying our theory for two-part fill factor resonant lattices based on the Rytov formulation are equivalently applicable to the more complex four-part grating design. Analogous formulations can be derived for the general case of multipart unit cell structures with no restrictions on symmetry.

CONCLUSIONS

In summary, we present Rytov refractive indices obtained by solving the exact Rytov formulation initially derived in 1956. In contradiction to past work, where effective medium theory returns a single effective index for a given device, the full formalism provides multiple solutions based on the multiple roots inherent therein. We interpret these solutions as pertaining directly to evanescent waves that drive the laterally propagating Bloch modes foundational to lattice resonance. The resonant reradiated Bloch modes experience wavelengthdependent refractive indices that are solutions of Rytov's closed-form expressions. Moreover, the full set of Rytov indices is directly applicable to design of periodic photonic devices, including metamaterials and metasurfaces. Their manifestation fully supports the diffractive-optics explanation of resonance device physics in terms of lateral leaky Bloch modes and guided-mode resonance. The cutoff wavelengths of the evanescent diffraction orders define their spectral region of dominance and interaction. The spectral slope of the Rytov indices predicts spectral ranges across which the reradiated Bloch modes will be in phase or out of phase. Thus, for example, it is possible to predict whether to expect a wideband reflector behavior from a one-dimensional grating structure simply by calculating effective refractive index graphs without performing any rigorous numerical simulations. The closedform Rytov formulas might thus substantiate efficient design methods. The fact that the cutoff wavelengths are directly embedded in the formulation enables definition of the dividing line between the resonance subwavelength region and the deep-subwavelength region based on the cutoff wavelength of the first evanescent diffraction order. This important transition point is always numerically available via the Rytov formulation. In a special case, we find that the transition wavelength is given by $\lambda_c^1 = 2Fn_H\Lambda$, which is directly comparable to the universal Rayleigh wavelength $\lambda_R = n_S \Lambda$ that defines transition from the nonsubwavelength to the subwavelength regime. We successfully apply the Rytov formalism to reliably describe the behavior of various optical devices, such as wideband reflectors, resonant bandpass filters, and guided-mode resonance polarizers. Rigorous numerical results support all of our explanations and predictions. Future studies might investigate and extend the methods of this study to more complex lattices such as those with multipart unit cells. Additionally, since the fundamental properties of the elemental 1D lattices studied here transfer in large measure to corresponding 2D lattices, extension of this work to 2D periodic metasurfaces is of interest. The utility and precision with which the simple Rytov formalism applies to resonant photonic lattices, including metamaterials, is an important discovery with potential to support future advances in the field.

AUTHOR INFORMATION

Corresponding Author

Robert Magnusson — Department of Electrical Engineering, University of Texas at Arlington, Arlington, Texas 76019, United States; © orcid.org/0000-0002-8584-0791; Email: magnusson@uta.edu

Author

Hafez Hemmati — Department of Electrical Engineering and Department of Materials Science and Engineering, University of Texas at Arlington, Arlington, Texas 76019, United States

Complete contact information is available at: https://pubs.acs.org/10.1021/acsphotonics.0c01244

Notes

The authors declare no competing financial interest.

ACKNOWLEDGMENTS

This research was supported, in part, by the UT System Texas Nanoelectronics Research Superiority Award funded by the State of Texas Emerging Technology Fund as well as by the Texas Instruments Distinguished University Chair in Nanoelectronics endowment. Additional support was provided by the National Science Foundation (NSF) under Award Nos. ECCS-1606898, ECCS-1809143, and IIP-1826966.

REFERENCES

- (1) Wood, R. W. On a remarkable case of uneven distribution of a light in a diffraction grating spectrum. *Philos. Mag.* **1902**, *4*, 396–402.
- (2) Rayleigh, L. Note on the remarkable case of diffraction spectra described by Prof. Wood. *Philos. Mag.* **1907**, *14*, 60–65.
- (3) Petit, R., Ed. In *Electromagnetic Theory of Gratings*; Springer-Verlag: Berlin, 1980.
- (4) Peng, S. T.; Bertoni, H. L.; Tamir, T. Analysis of periodic thinfilm structures with rectangular profiles. *Opt. Commun.* **1974**, *10*, 91– 94
- (5) Moharam, M. G.; Gaylord, T. K. Diffraction analysis of dielectric surface-relief gratings. *J. Opt. Soc. Am.* **1982**, *72*, 1385–1392.
- (6) Vincent, P.; Neviere, M. Corrugated dielectric waveguides: A numerical study of the second-order stop bands. *Appl. Phys.* **1979**, *20*, 345–351.
- (7) Popov, E.; Mashev, L.; Maystre, D. Theoretical study of the anomalies of coated dielectric gratings. *Opt. Acta* **1986**, *33*, 607–619.
- (8) Avrutsky, I. A.; Svakhin, A. S.; Sychugov, V. A. Interference phenomena in waveguides with two corrugated boundaries. *J. Mod. Opt.* **1989**, *36*, 1303–1320.
- (9) Wang, S. S.; Magnusson, R. Theory and applications of guided-mode resonance filters. *Appl. Opt.* **1993**, *32*, 2606–2613.
- (10) Lalanne, P.; Hugonin, J. P.; Chavel, P. Optical properties of deep lamellar gratings: a coupled Bloch-mode insight. *J. Lightwave Technol.* **2006**, 24, 2442–2449.
- (11) Chang-Hasnain, C. J.; Yang, W. High-contrast gratings for integrated optoelectronics. *Adv. Opt. Photonics* **2012**, *4*, 379–440.
- (12) Fattal, D.; Li, J.; Peng, Z.; Fiorentino, M.; Beausoleil, R. G. Flat dielectric grating reflectors with focusing abilities. *Nat. Photonics* **2010**, *4*, 466–470.
- (13) Zhang, B.; Wang, Z.; Brodbeck, S.; Schneider, C.; Kamp, M.; Hofling, S.; Deng, H. Zero-dimensional polariton laser in a subwavelength grating-based vertical microcavity. *Light: Sci. Appl.* **2014**, *3*, No. e135.
- (14) Quaranta, G.; Basset, G.; Martin, O. J. F.; Gallinet, B. Recent advances in resonant waveguide gratings. *Laser Photonics Rev.* **2018**, *12*, 1800017.
- (15) Kildishev, A. V.; Boltasseva, A.; Shalaev, V. M. Planar photonics with metasurfaces. *Science* **2013**, 339 (6125), 1232009.

- (16) Desiatov, B.; Mazurski, N.; Fainman, Y.; Levy, U. Polarization selective beam shaping using nanoscale dielectric metasurfaces. *Opt. Express* **2015**, 23 (17), 22611–22618.
- (17) Arbabi, A.; Horie, Y.; Bagheri, M.; Faraon, A. Dielectric metasurfaces for complete control of phase and polarization with subwavelength spatial resolution and high transmission. *Nat. Nanotechnol.* **2015**, *10*, 937–943.
- (18) Holsteen, A. L.; Cihan, A. F.; Brongersma, M. L. Temporal color mixing and dynamic beam shaping with silicon metasurfaces. *Science* **2019**, 365 (6450), 257–260.
- (19) Jahani, S.; Jacob, Z. All-dielectric metamaterials. *Nat. Nanotechnol.* **2016**, *11*, 23-36.
- (20) Rytov, S. M. Electromagnetic properties of a finely stratified medium. *Sov. Phys. JETP* **1956**, 2 (3), 466–475.
- (21) Gaylord, T. K.; Baird, W. E.; Moharam, M. G. Zeroreflectivity high spatial-frequency rectangular-groove dielectric surface-relief gratings. *Appl. Opt.* **1986**, *25*, 4562–4567.
- (22) Ono, Y.; Kimura, Y.; Ohta, Y.; Nishida, N. Antireflection effect in ultrahigh spatial-frequency holographic relief gratings. *Appl. Opt.* **1987**, 26, 1142–1146.
- (23) Richter, I.; Sun, P. C.; Xu, F.; Fainman, Y. Design considerations of form birefringent microstructures. *Appl. Opt.* **1995**, 34, 2421–2429.
- (24) Raguin, D.; Morris, G. M. Antireflection structured surfaces for the infrared spectral region. *Appl. Opt.* **1993**, *32*, 1154–1167.
- (25) Tang, S. W.; Zhu, B. C.; Jia, M.; He, Q.; Sun, S. L.; Mei, Y. F.; Zhou, L. Effective-medium theory for one-dimensional gratings. *Phys. Rev. B: Condens. Matter Mater. Phys.* **2015**, *91*, 174201.
- (26) Lalanne, P.; Lemercier-Lalanne, D. On the effective medium theory of subwavelength periodic structures. *J. Mod. Opt.* **1996**, *43*, 2063–2085.
- (27) Lalanne, P.; Hugonin, J. P. High-order effective-medium theory of subwavelength gratings in classical mounting: application to volume holograms. *J. Opt. Soc. Am. A* **1998**, *15* (7), 1843–1851.
- (28) Isaacs, S.; Hajoj, A.; Abutoama, M.; Kozlovsky, A.; Golan, E.; Abdulhalim, I. Resonant grating without a planar waveguide layer as a refractive index sensor. *Sensors* **2019**, *19*, 3003.
- (29) Kikuta, H.; Yoshida, H.; Iwata, K. Ability and limitation of effective medium theory for subwavelength gratings. *Opt. Rev.* **1995**, 2, 92–99.
- (30) Rosenblatt, D.; Sharon, A.; Friesem, A. A. Resonant grating waveguide structures. *IEEE J. Quantum Electron.* **1997**, 33, 2038–2059.
- (31) Ding, Y.; Magnusson, R. Resonant leaky-mode spectral-band engineering and device applications. *Opt. Express* **2004**, *12*, 5661–5674
- (32) Ko, Y. H.; Magnusson, R. Wideband dielectric metamaterial reflectors: Mie scattering or leaky Bloch mode resonance? *Optica* **2018**, *5*, 289–294.
- (33) Gaylord, T. K.; Moharam, M. G. Analysis and applications of optical diffraction by gratings. *Proc. IEEE* **1985**, 73 (5), 894–937.
- (34) Moharam, M. G.; Gaylord, T. K. Diffraction analysis of dielectric surface-relief gratings. J. Opt. Soc. Am. 1982, 72, 1385–1392.
- (35) Moitra, P.; Slovick, B. A.; Yu, Z. G.; Krishnamurthy, S.; Valentine, J. Experimental demonstration of a broadband all-dielectric metamaterial perfect reflector. *Appl. Phys. Lett.* **2014**, *104*, 171102.
- (36) Karagodsky, V.; Sedgwick, F. G.; Chang-Hasnain, C. J. Theoretical analysis of subwavelength high contrast grating reflectors. *Opt. Express* **2010**, *18* (16), 16973–16988.
- (37) Mateus, C. F. R.; Huang, M. C. Y.; Chen, L.; Chang-Hasnain, C. J.; Suzuki, Y. Broad-band mirror (1.12–1.62 μ m) using a subwavelength grating. *IEEE Photonics Technol. Lett.* **2004**, *16* (7), 1676–1678.
- (38) Magnusson, R.; Shokooh-Saremi, M. Physical basis for wideband resonant reflectors. *Opt. Express* **2008**, *16* (5), 3456–3462.
- (39) Heo, H.; Lee, S.; Kim, S. Tailoring fano resonance for flat-top broadband reflectors based on single guided-mode resonance. *J. Lightwave Technol.* **2019**, *37*, 4244–4250.

- (40) Jin, W.; Li, W.; Orenstein, M.; Fan, S. Inverse design of lightweight broadband reflector for relativistic lightsail propulsion. *ACS Photonics* **2020**, *7* (9), 2350–2355.
- (41) Tibuleac, S.; Magnusson, R. Narrow-linewidth bandpass filters with diffractive thin-film layers. *Opt. Lett.* **2001**, *26*, 584–586.
- (42) Ding, Y.; Magnusson, R. Doubly-resonant single-layer bandpass optical filters. *Opt. Lett.* **2004**, *29*, 1135–1137.
- (43) Foley, J. M.; Young, S. M.; Phillips, J. D. Narrowband mid-infrared transmission filtering of a single layer dielectric grating. *Appl. Phys. Lett.* **2013**, *103*, No. 071107.
- (44) Niraula, M.; Yoon, J. W.; Magnusson, R. Mode-coupling mechanisms of resonant transmission filters. *Opt. Express* **2014**, 22 (21), 25817–25829.
- (45) Delbeke, D.; Baets, R.; Muys, P. Polarization-selective beam splitter based on a highly efficient simple binary diffraction grating. *Appl. Opt.* **2004**, *43*, 6157–6165.
- (46) Yoon, J. W.; Lee, K. J.; Magnusson, R. Ultra-sparse dielectric nanowire grids as wideband reflectors and polarizers. *Opt. Express* **2015**, 23, 28849–28856.
- (47) Pecora, E. F.; Cordaro, A.; Kik, P. G.; Brongersma, M. L. Broadband antireflection coatings employing multiresonant dielectric metasurfaces. *ACS Photonics* **2018**, *5* (11), 4456–4462.
- (48) Lin, D.; Melli, M.; Poliakov, E.; Hilaire, P. S.; Dhuey, S.; Peroz, C.; Cabrini, S.; Brongersma, M. L.; Klug, M. Optical metasurfaces for high angle steering at visible wavelengths. *Sci. Rep.* **2017**, *7* (1), 2286.
- (49) Ilic, O.; Atwater, H. A. Self-stabilizing photonic levitation and propulsion of nanostructured macroscopic objects. *Nat. Photonics* **2019**, *13* (4), 289–295.